ORIGINAL RESEARCH ARTICLE

The Potential of High-Velocity Air-Fuel Spraying (HVAF) to Manufacture Bond Coats for Thermal Barrier Coating Systems

Georg Mauer[1] · Karl-Heinz Rauwald[1] · Yoo Jung Sohn[1] · Robert Vaßen[1]

Abstract Driven by the search for an optimum combination of particle velocity and process temperature to achieve dense hard metal coatings at high deposition efficiencies and powder feed rates, the high-velocity air-fuel spraying process (HVAF) was developed. In terms of achievable particle velocities and temperatures, this process can be classified between high-velocity oxy-fuel spraying (HVOF) and cold gas spraying (CGS). The particular advantages of HVAF regarding moderate process temperatures, high particle velocities as well as high productivity and efficiency suggest that the application of HVAF should be also investigated for the manufacture of MCrAlY (M = Co and/or Ni) bond coats (BCs) in thermal barrier coating (TBC) systems. In this work, corresponding HVAF spray parameters were developed based on detailed process analyses. Different diagnostics were carried out to characterize the working gas jet and the particles in flight. The coatings were investigated with respect to their microstructure, surface roughness and oxygen content. The spray process was assessed for its effectiveness. Process diagnostics as well as calculations of the gas flow in the jet and the particle acceleration and heating were applied to explain the governing mechanisms on the coating characteristics. The results show that HVAF is a promising alternative manufacturing process.

Keywords bond coat (BC) · cold gas spraying (CGS) · high-velocity air-fuel spraying (HVAF) · high-velocity oxy-fuel spraying (HVOF) · thermal barrier coating (TBC)

✉ Georg Mauer
g.mauer@fz-juelich.de

1   Forschungszentrum Jülich GmbH, Institute of Energy and Climate Research, IEK-1: Materials Synthesis and Processing, Jülich, Germany

Introduction

The relatively new kinetic spray processes high-velocity oxy-fuel spraying (HVOF) and cold gas spraying (CGS) enabled major advances in manufacturing dense and well-adhering metallic coatings with high deposition rates (Ref 1). However, there are specific disadvantages regarding the processing of hard metals. These are hard materials commonly using W, Cr or Ti carbide particles dispersed in a metallic matrix, e.g., of Co, Ni, Cr and/or Ti. When HVOF spraying such materials, decarburization, oxidation and dissolution leading to the formation of undesired phases can occur due to the relative high processing temperatures (Ref 2). In CGS of such hard metals, the bonding mechanism is by high strain rates due to adiabatic shear instabilities mainly at the interface of binder particles. In particular at low metallic binder contents, the deposition efficiency and the coating density can be affected. Cold-sprayed WC-Co coatings were mostly achieved by using expensive compressed high-temperature helium as propulsive gas or using nitrogen combined with powder

preheating treatment to thermally soften Co matrix phase. Apart from these two methods, deposition of WC-Co coatings using solely nitrogen as working gas was seldom reported (Ref 3).

One approach to address these problems is warm spraying (WS), which is a modified HVOF process. Here, the temperature of the working gas is controlled by injecting room temperature inert gas (nitrogen) into the combustion gas jet (Ref 4). However, in case of WC-Co powders, the deposition efficiencies were reported to be quite low (Ref 5).

Driven by the search for an optimum combination of particle velocity and process temperature to achieve dense hard metal coatings at high deposition efficiencies and powder feed rates (Ref 2), the high-velocity air-fuel spraying process (HVAF) was developed (Ref 6). In terms of achievable particle velocities and temperatures, this process can be classified between HVOF and CGS. Like HVOF and WS, HVAF utilizes the energy of a supersonic velocity jet formed by the combustion of a gaseous fuel, however using air as oxidizer gas instead of oxygen. Propane (C_3H_8) is typically used as fuel gas, but propylene (C_3H_6) or methane (CH_4) can be used as alternatives providing higher and lower flame temperatures, respectively. The maximum temperature in the combustion chamber can reach 1900-1950 °C at a pressure up to 0.6-0.8 MPa. Here, the powder material is axially injected, from where it passes into the accelerating nozzle. The particles are often just thermally softened, i.e., not heated up to the melting point, thus remaining in a solid or a semi-solid state. However, for hard metals it is recommended to have the matrix material at deposition in liquid phase (Ref 6). Besides wear-resistant coatings, corrosion protection (e.g., Ni-Cr or Ni-Al alloys) is an important application field of HVAF coatings (Ref 7). HVAF shows a high productivity allowing spraying up to approx. 500 g min^{-1} of WC-based powders, while deposition efficiencies were reported to reach 70% (Ref 8). High deposition efficiencies were found to be maintained even at changing spray angles which was explained by the very high particle velocities. Thus, the process appears to be quite versatile (Ref 9). The high particle velocities are also advantageous as any oxide layers present are effectively broken up. Besides, the deposition efficiency was found to be improved if the substrate temperature was increased (Ref 10).

The particular advantages of HVAF regarding moderate process temperatures, high particle velocities as well as high productivity suggest the application of HVAF generally for corrosion and oxidation protective coatings. In this work, HVAF was investigated for the manufacture of MCrAlY (M = Co and/or Ni) bond coats (BCs). As first layer in thermal barrier coating systems (TBCs), they provide for a good adhesion of the heat-insulating oxide ceramic top coats and protect metallic gas turbine components such as airfoils, blades and shrouds against corrosive attack by oxidation and sulfidation at high temperatures. During operation, they generate a protective oxide scale (thermally grown oxide, TGO) that retards such chemical attack. A post-coating heat treatment promotes the formation of corrosion-resistant intermetallics and further densifies the coating, thereby enhancing its protective characteristics.

In this work, HVAF was tried as an alternative manufacturing method for BCs as the already established procedures each have specific disadvantages. Low-pressure plasma spraying (LPPS, formerly often referred to as vacuum plasma spraying, VPS) is expensive. High-velocity oxy-fuel spraying (HVOF) involves a certain oxygen uptake, which may be undesirable. Consequently, the formation of Al-rich oxides lowers the metallic Al concentration, which is available for diffusion and TGO formation. This is generally assumed to affect the oxidation resistance adversely. It is even more pronounced with atmospheric plasma spraying (APS). In CGS, very high working gas pressures and temperatures are needed for BCs to achieve dense coatings with high deposition efficiencies. Thus, HVAF may be an economical alternative.

Experimental Methods and Materials

Spray work was carried out in the Jülich Thermal Spray Center (JTSC) (Ref 11) on a HVAF system with an UltraCoat™ process controller in combination with a M3™ supersonic spray gun mounted on a six-axis industrial robot and a G4™ gravimetric powder feeder (Uniquecoat Technologies, LLC, Oilville, VA, USA). The air-cooled spray gun was operated on propane as fuel gas. Inside, a finely perforated flame holder (Ref 12), which also has a catalytic function (Ref 13), provides an effective combustion of the primary air-fuel mixture. A dual-nozzle system allows additionally the combustion of secondary fuel that is fed separately from the primary fuel, mixed with part of the air and fed into the gas jet originating from the primary combustion (Ref 14). This kind of afterburning compensates for thermal losses and increases the jet temperature so that longer nozzles can be applied compared to single-nozzle systems.

A special feature of the HVAF system used in this work was the equipment with mass flow gauges in the compressed air supply and the two fuel lines. These flows are pressure regulated. Thus, the actual mass flows on the one hand depend on the individual configuration of the system, e.g., on tube lengths, fittings, manifolds and valves. On the other hand, there are interactions between the single gas flows. This means that if the pressure is lifted in one line to

increase this flow, the other flows will decrease somewhat, because their pressures are controlled to maintain constant values. However, the pressure in the combustion chamber against which the process gases are fed increases. This makes process development somewhat tricky and complicates the transfer of parameter sets from one system to another.

The interactions between the gas flows are reflected quantitatively by standardized effect estimates of the airflow, fuel 1 flow, fuel 2 flow, and the combustion chamber pressure given in Table 1, resulting from a multivariate linear regression with air, fuel 1, and fuel 2 pressures as factors. Due to the standardization, the relative impact of the factors can be identified by direct comparison. The last column of Table 1 gives the coefficients of determination of the models for each effect. The regression polynomials can also be used to specifically calculate air and fuel pressures that realize specified gas flows. However, it should be noted that these regression coefficients are valid only for the particular spray system in Jülich.

The powder material is axially injected into the combustion chamber, from where it passes into the accelerating nozzle. Two convergent-divergent ceramic nozzles were used alternatively, type 4L2 with an expansion ratio of 1.36 and type 4L4 with an expansion ratio of 1.78. With these nozzle geometries, increasing particle velocities and decreasing particle temperatures can be expected as the expansion ratio increases (Ref 15). The powder stream was narrower than the gas jets formed in the applied nozzles so that the particles were shrouded along their flight (Fig. 1).

The photographs of the jet appearance in this study were taken with a Nikon D 500 digital camera equipped with a 60-mm/F 2.8 lens (corresponds to 90 mm in 35-mm film). The exposure time was 0.05 s, the ISO sensitivity was 1000, and the aperture was F 5.6 and F 3.5 for the 4L2 and the 4L4 nozzle, respectively. The brightness distributions of some photographs were transformed to rainbow pseudocolors using the GNU image manipulation software GIMP (v. 2.10.32).

Particle velocities were measured by means of a cold spray meter CSM EVOLUTION (Tecnar Automation Inc. St. Bruno. QC, Canada) which corresponds to the velocity measurement partial system of the well-known DPV-2000, additionally equipped with a continuous diode laser source to illuminate the particle plume (wavelength 790 nm, power 3.3W, divergence 70 mrad). The sensor collects the light scattered close to the laser direction. Such scattering configuration minimizes the influence of the particle size on the measured particle diameter and maximizes the scattered light intensity (Ref 16). More details can be found elsewhere (Ref 17).

Gas velocity measurements were taken by means of a set of two Pitot tubes. The tubes could not be used at spray distances shorter than 275 mm because of the risk of overheating. In the case of a continuum supersonic freestream, a probe of finite size will cause the formation of a detached shock; hence, a total pressure probe will measure the reduced stagnation pressure in the decelerated subsonic flow behind the shock front. Because of the non-isentropic nature of the compression through the shock wave, the Bernoulli equation cannot be used. However, the freestream Mach number can be found by means of the Rayleigh supersonic pitot formula (Ref 18), whereby the solution is obtained iteratively. The freestream static pressure and the static and dynamic pressures behind the bow shock were measured. The stagnation temperature was also measured there by an integrated thermocouple. Values of the gas properties used in the Rayleigh equation (specific heat ratio, molar mass and sound velocity) were calculated for different temperatures using the CEA software (Ref 19, 20) assuming chemical equilibrium, fitted and interpolated for the measured gas temperatures. The rocket feature of the same program was used to calculate the gas
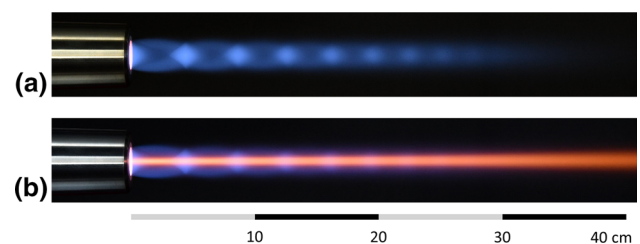

Fig. 1 HVAF supersonic jets formed by the 4L2 nozzle, (a) without powder injection, (b) with injection of 20 g/min MCrAlY powder

Table 1 Standardized effect estimates for the airflow, fuel 1 flow, fuel 2 flow and the combustion chamber pressure resulting from a multivariate linear regression with air, fuel 1 and fuel 2 pressures as factors; the last column gives the coefficients of determination of the models

	Air pressure	Fuel 1 pressure	Fuel 2 pressure	Coefficient of determination R^2
Air mass flow	0.64	− 0.70	− 0.33	0.98
Fuel 1 mass flow	− 0.26	0.90	− 0.25	0.94
Fuel 2 mass flow	− 0.09	− 0.15	0.97	0.99
Combustion chamber pressure	0.46	0.83	0.51	0.97

velocities and other properties at the nozzle exit cross sections.

One MCrAlY powder with the composition of Co 32Ni 21Cr 8Al 0.5Y was used showing the typical spherical morphology of gas-atomized particles, namely Amdry 9954 with a nominal sieve fraction of $- 63/ + 11$ μm (Oerlikon Metco Europe, Kelsterbach, Germany). Table 2 gives the actual characteristic particle diameters measured by laser diffraction (LA-950, Horiba Europe, Oberursel, Germany). The powder feed rate was 50 g min^{-1}, and the carrier gas flow was 45 standard liters per minute (slpm).

The spray parameters used in this study are given in Table 3. The gun was more sensitive to changes in air and fuel 1 flow compared to variations of the fuel 2 setting. Since the window of the air/fuel ratio was rather narrow for a stable gun operation (Ref 21), the gas flows were not varied, but only the spray distance. λ is the air-fuel equivalence ratio normalized by the stoichiometric case calculated for the overall air and fuel flows. λ may vary considerably at different locations in the combustion chamber and the nozzle. Using the 4L2 nozzle, a stable jet formation was found down to an air-fuel equivalence ratio of $\lambda = 1.30$. For the 4L4 nozzle, this threshold was found at $\lambda = 1.25$.

Figure 2 gives the composition of the combustion gas calculated by CEA (equilibrium conditions assumed). Since the air-fuel mixture is rather lean, the combustion is complete. Only small traces of CO, H, H_2, OH as well as of NO_x are present.

Figure 3 shows the adiabatic flame temperatures of the combustion gas calculated by CEA as a function of the normalized air-fuel equivalence ratio λ (equilibrium conditions assumed). Typically, the maximum temperature is found on the fuel-rich side slightly below the stoichiometric case at $\lambda < 1.0$. The ranges in which the torch could be operated stably with the two nozzles are indicated. The impact of the pressure in the combustion chamber on the temperature was small. A pressure in the combustion chamber of approx. 0.6 MPa was measured in this study.

Test samples were manufactured from stainless steel (AISI 316Ti) with dimensions of Ø 30 × 5 mm. They were grit-blasted with an air pressure of 0.25 MPa using high-grade corundum with a F36 grain size (425-600 μm), which led to an arithmetic mean roughness of $R_a \approx 4$ μm.

Scanning electron microscope investigations (SEM) were accomplished by an Ultra55 model (Carl Zeiss NTS

Table 3 HVAF spray parameters used in this study

		4L2 nozzle	4L4 nozzle
Air	0.814 MPa (118 psi)	7.75 sm^3/min	8.38 sm^3/min
Fuel 1	0.689 MPa (100 psi)	0.30 kg/min	0.34 kg/min
Fuel 2	0.724 MPa (105 psi)	0.18 kg/min	0.20 kg/min
λ		1.31	1.26
Spray dist.	275/350/425 mm		
Robot vel.	1000 mm/s		
Raster	1 mm		

psi: pounds per square inches
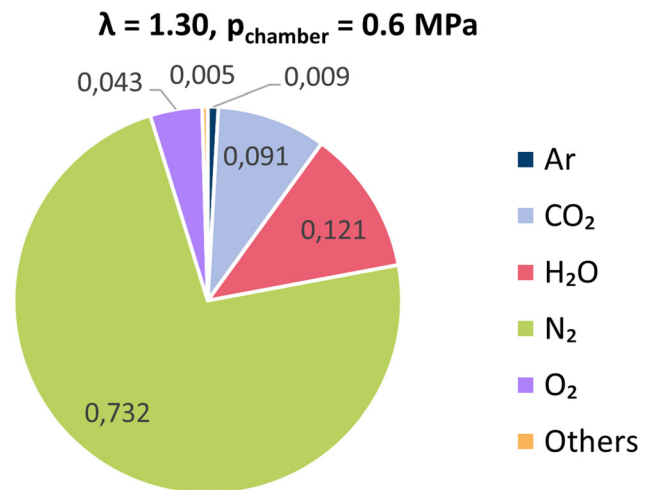
sm^3: standard cubic meter

Fig. 2 Calculated composition (mol%) of the combustion gas (equilibrium conditions assumed)
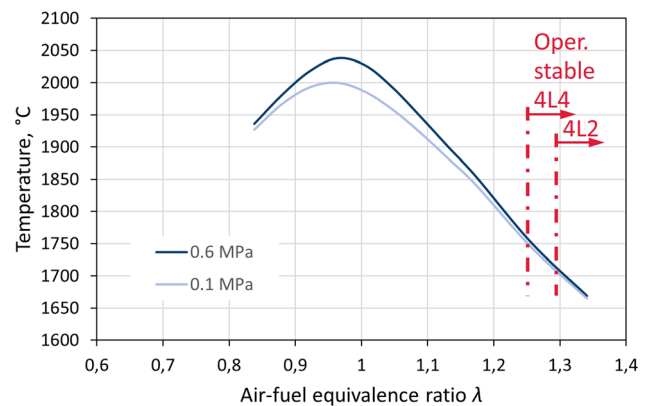

Fig. 3 Calculated adiabatic flame temperatures of the combustion gas as a function of the normalized air-fuel equivalence ratio λ (equilibrium conditions assumed)

GmbH, Oberkochen, Germany). For SEM examination, the samples were coated with approximately 2-nm platinum. Microstrain and phase analyses by x-ray diffractometry
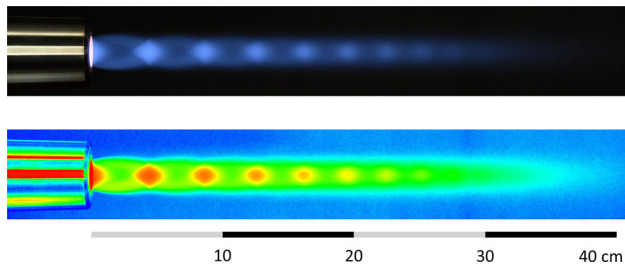
Table 2 Characteristic diameters of the used CoNiCrAlY powders

d_{10}, μm	20
d_{50}, μm	30
d_{90}, μm	44

Fig. 4 HVAF jet appearance using the 4L2 nozzle in true colors (top) and converted to rainbow pseudocolors (bottom)

were carried out by means of the D4 Endeavor system (Bruker AXS, Karlsruhe, Germany) applying the focusing Bragg-Brentano (BB) geometry. All XRD scans were taken using Cu-K$_\alpha$ radiation (40 kV, 40 mA) at Bragg angles 2θ between 10° and 80°, with increments of 0.02° and a scan time of 0.75 s/step. Thereafter, the data were analyzed using the TOPAS software V4.2 (general profile and structure analysis software for powder diffraction data, Bruker AXS, Karlsruhe, Germany). It enables the determination of physically meaningful microstructure parameters based on the accurate discrimination between instrument and individual specimen contributions to an XRD pattern (fundamental parameters approach). Among others, these parameters comprise residual stresses.

Results and Discussion

Jet Appearance

Figure 4 shows the HVAF jet appearance using the 4L2 nozzle in true colors and in the brightness converted to rainbow pseudocolors. It is obvious that the jet is underexpanded and thus expands spontaneously upon exiting the nozzle. The resulting expansion wave is reflected several times at the edges of the jet forming the characteristic sequence of expansion and compression cells (Mach diamonds) in a supersonic jet.

This is different if the 4L4 nozzle is used, Fig. 5. Due to its larger expansion ratio, the jet in the nozzle is almost expanded to the ambient pressure so that Mach diamonds are only slightly pronounced.

Gas and Particle Velocities

Figure 6 shows gas and particle velocities for the 4L2 and the 4L4 nozzle measured by the Pitot tube set and by the cold spray meter at different spray distances. The velocity differences using the two nozzles are not large. Obviously,
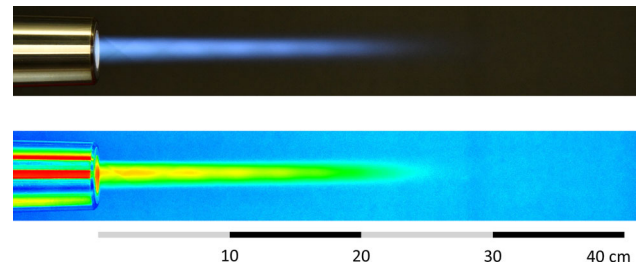

Fig. 5 HVAF jet appearance using the 4L4 nozzle in true colors (top) and transformed to rainbow pseudocolors (bottom)
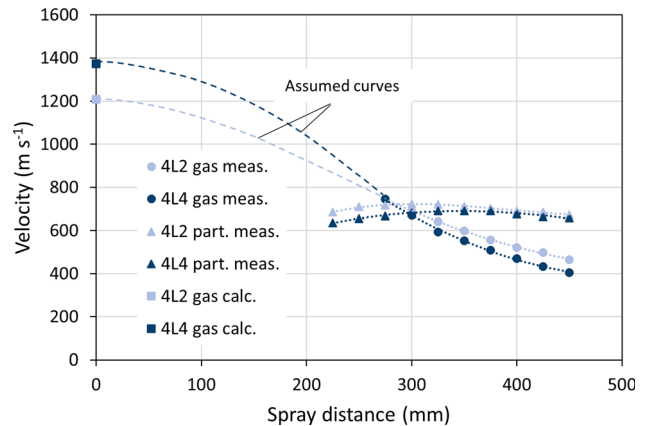

Fig. 6 Gas and particle velocities for the 4L2 and the 4L4 nozzle at different spray distances measured by a Pitot tube setup and by the cold spray meter; calculated gas velocities at the nozzle exits

the sequence of compression and expansion cells with the 4L2 nozzle, which are not observed with the 4L4 nozzle, does not affect the overall particle acceleration too much. The curves of gas and particle velocities should intersect where the particle velocities exhibit their maximum. At this spray distance, the relative velocity between gas and particles changes its sign and thus the particles are no more accelerated but retarded. This is approximately the case here. It should be noted that the gas and particle velocity curves were, after all, determined using two completely independent measurement methods.

Already the appearance of the particle jet shown in Fig. 1 suggests that the variation of particle properties in the investigated range of spray distance between 275 and 425 mm is not large. In contrast to the particles, no statement can be made here about the gas flow due to its low luminescence.

In addition, the gas velocities calculated for the nozzle exit cross sections are plotted in Fig. 6. Moreover, the calculated and measured gas velocities in Fig. 6 were linked by assumed curves with typical characteristics for high-kinetic spray processes with convergent-divergent nozzles (Ref 22). For the 4L4 nozzle with the larger expansion ratio, the gas velocity at the nozzle exit is

typically larger than for the 4L2 nozzle. But this alone does not mean that the acceleration of the particles is also higher there.

Considering other local gas properties such as density and viscosity (calculated by the CEA software), the drag force on a spherical particle with a diameter of 30 μm (median of the particle size distribution used in this study) was estimated using the approach of Cheng (Ref 23). This was done at three positions: (a) at an intermediate position between combustion chamber and nozzle throat, (b) at the nozzle exit and (c) in the free jet expanded to 70 kPa. Table 4 gives a comparison of results for the 4L2 and the 4L4 nozzle. It is evident that the drag force at the nozzle exit of the 4L2 nozzle is 22% higher than in the 4L4 nozzle. More downstream in the expanded jet, they are on the same level. Hence, it is logical that higher particle velocities were measured for the 4L2 nozzle.

Formation of Microstructures

Figure 7 shows an example for microstructures as sprayed with the 4L4 nozzle at 350-mm spray distance. It is obvious that the particles were only partly molten. Nevertheless, the porosity is small, see below. This is an indication of the highly kinetic conditions prevailing in the HVAF process.

In Fig. 8, single-splat morphologies sprayed with the 4L2 nozzle on mirror-polished stainless-steel substrates at 350-mm spray distance are shown. It is evident that the smaller particles were fully molten. Medium-sized particles were semi-molten, while the largest particles were just thermally softened. The semi-molten state may also occur due to the coexistence of liquid and solid phase as the MCrAlY alloys of the Amdry 995 family do not melt
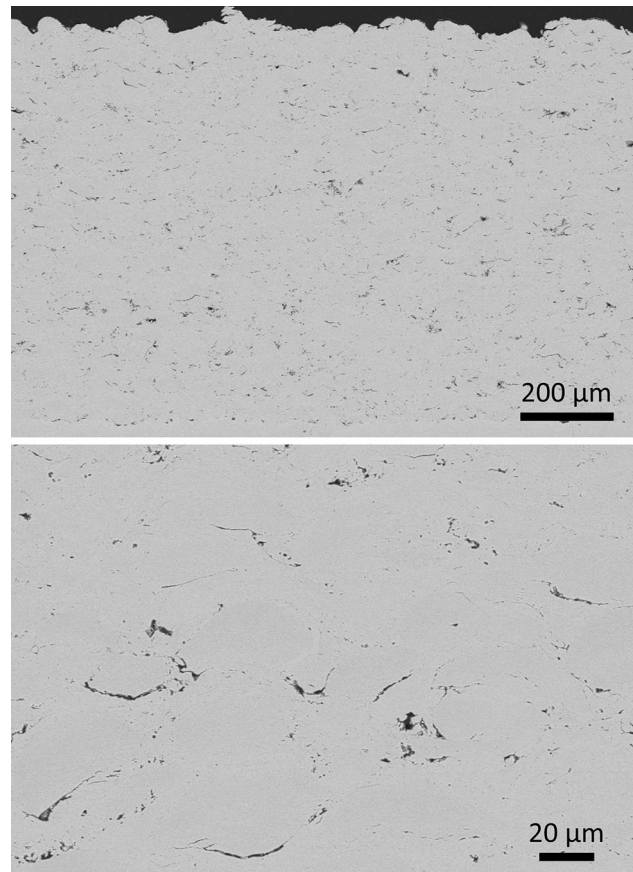

Fig. 7 Example for cross sections of microstructures as sprayed with the 4L4 nozzle at 350-mm spray distance (backscattered electron images)

Table 4 Comparison of the drag forces on a spherical particle with a diameter of 30 μm using the 4L2 and the 4L4 nozzles and at three positions

	(a) Chamber/throat	(b) Nozzle exit	(c) Expanded jet, 70 kPa	
4L2				
ρ_g	1.08	0.40	0.21	kg m^{-3}
Re	244	87	52	…
C_D	0.73	1.18	1.56	…
4L4				
ρ_g	1.11	0.28	0.20	kg m^{-3}
Re	201	65	50	…
C_D	0.79	1.38	1.59	…
$F_D^{(4L2)}/F_D^{(4L4)}$	0.89	1.22	1.0	…

(a) At an intermediate position between combustion chamber and nozzle throat

(b) At the nozzle exit

(c) In the free jet expanded to 70 kPa

ρ_g is the gas density, Re is the Reynolds number, C_D is the drag coefficient, and F_D is the drag force.
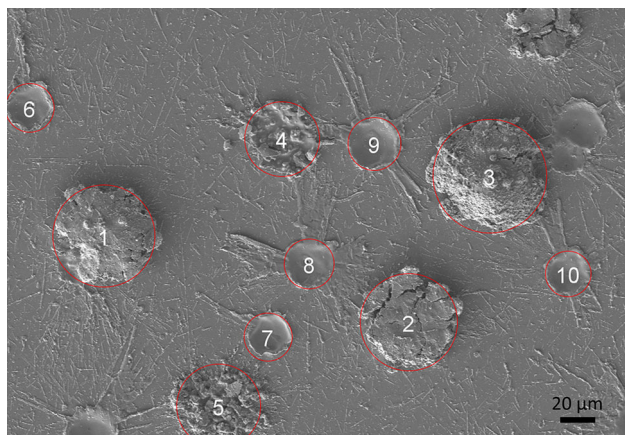
Fig. 8 Single-splat morphologies sprayed with the 4L2 nozzle on mirror-polished stainless-steel substrates at 350-mm spray distance: softened No. 1-3, splat Ø 56-66 µm; semi-molten No. 4 and 5, splat Ø 43-48 µm; fully molten No. 6-10, splat Ø 26-31 µm; (secondary electron image)

Table 5 Calculated melting indices I_m for the three characteristic particle diameters d_{10}, d_{50} and d_{90} and the solidus and the liquidus temperatures T_m for the Amdry 995 family; the nozzle type was 4L2 and the spray distance 350 mm; d_p is the particle diameter, Re is the Reynolds number, Pr is the Prandtl number, Nu is the Nusselt number, h_c is the convective heat transfer coefficient, and Bi is the Biot number

	d_{10}	d_{50}	d_{90}	
d_p	20	30	44	µm
Re	163	244	358	…
Δt_{fly}	0.75	1.01	1.31	ms
Pr	0.735	…		
Nu	8.9	10.5	12.2	…
h_c	$5.6 \cdot 10^4$	$4.4 \cdot 10^4$	$3.5 \cdot 10^4$	W m^{-2} K^{-1}
Bi	0.11	0.13	0.15	…
$T_{m,\ liquidus}$	1703	K		
Δt_m	0.61	1.18	2.28	ms
$I_m = \Delta t_{fly}/\Delta t_m$	1.23	0.85	0.60	…
$T_{m,\ solidus}$	1635	K		
Δt_m	0.48	0.92	1.71	ms
$I_m = \Delta t_{fly}/\Delta t_m$	1.57	1.09	0.77	…

congruently (Ref 24). The different degrees of melting determine the formation of the sprayed microstructures and thus the porosity and the surface roughness of the coatings.

The influence of the particle diameter on the melting degree can be understood by calculating the so-called melting index I_m. The calculation is based on the ratio of the time of particle flight Δt_{fly} to the time Δt_m which is necessary to melt the particle to the core. $I_m > 1.0$ means that the particle can be completely melted before impacting
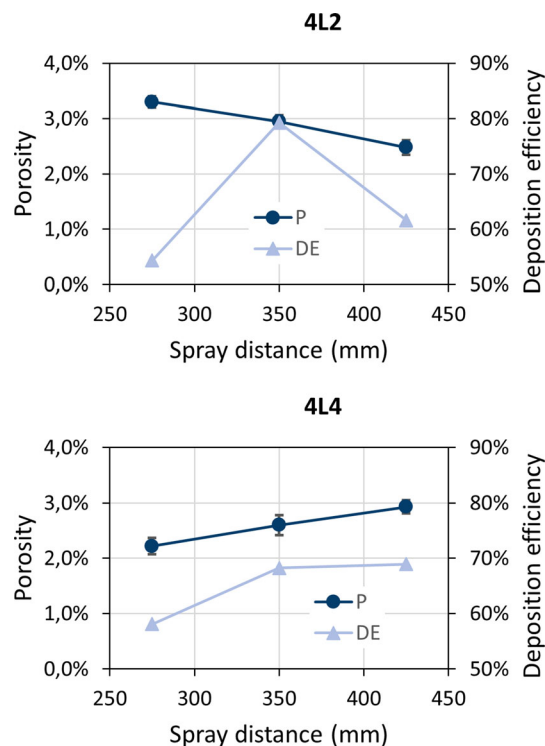

Fig. 9 Porosities P and deposition efficiencies DE of samples sprayed at different spray distances with the 4L2 and the 4L4 nozzle, respectively

on the substrate. More details of the calculation can be found elsewhere (Ref 25). Table 5 gives the calculation results for the three characteristic particle diameters d_{10}, d_{50} and d_{90}. Two temperatures T_m were taken, the solidus and the liquidus temperature for the Amdry 995 family according to (Ref 26). The particle flight path was from the powder injector in the combustion chamber of the gun to the nozzle throat; the nozzle type was 4L2.

It is evident that the largest particle with d_{90} cannot be completely molten as $I_m < 1$. For the particles with the median diameter d_{50}, the solidus temperature can reach in the core, but not the liquidus temperature. The smallest particles with d_{10} can be melted completely to the core. Thus, the different observed splat morphologies shown in Fig. 8 can be well explained.

Porosity

The porosities of samples sprayed at different spray distances with the 4L2 and the 4L4 nozzle, respectively, are shown in Fig. 9. They were determined by digital image analysis. The error bars represent standard deviations for the individual data points resulting from four analyzed SEM images each. The overall porosity range between 2 and 3.5% corresponds to what is attained by LPPS (Ref 27)

and HVOF (Ref 28, 29) and is better than what is typically achieved by CGS (Ref 30).

Deposition Efficiency

In particular in porous ceramic coatings, the deposition efficiency often performs inversely to the porosity (Ref 31). However, such correlation could not be found in this study, cp. Fig. 9. The best DE values reached 70-80% at spray distances of 350 mm and above; for the 4L2 nozzle, there was already a drop again at 425 mm. It is suggested that on the one hand, a minimum dwell time in the hot gas jet is required to achieve sufficient melting degrees; on the other hand, the flight path should not be too long to avoid particle cooling at larger spray distances.

Surface Roughness

Figure 10 shows the arithmetic mean roughness values R_a on sample surfaces sprayed at different spray distances obtained with the 4L2 and the 4L4 nozzle, respectively. They were determined by optical profilometry. Experience shows that a minimum roughness of $R_a \approx 6$ μm is required to ensure good adhesion of ceramic thermal barrier coatings to the bond coat. Although R_a values are not

Fig. 10 Arithmetic mean roughness R_a on sample surfaces sprayed at different spray distances with the 4L2 and the 4L4 nozzle, respectively; the error range of these measurements was smaller than 1%

sufficient to describe the bonding completely, the values between 9 and 11 μm achieved here by HVAF are expected to be favorable.

Oxygen Content

The oxygen contents of two freestanding samples sprayed at 350 mm were determined by inductively coupled plasma optical emission spectrometry (ICP-OES). The coating sprayed with the 4L2 nozzle exhibited 0.246 ± 0.005 wt.% oxygen, while the coating sprayed with the 4L4 nozzle contained 0.228 ± 0.001 wt.%. In the author's experience, the feedstock powder contains approx. 0.04 wt.% oxygen (Ref 27). Hence, a certain oxygen uptake must have occurred during particle flight and on the hot substrate surface immediately after deposition. However, this is very moderate if compared to other thermal spray processes carried out under atmospheric conditions, such as HVOF or particularly APS; some reference values can be found elsewhere (Ref 32).

Residual Stresses

Residual strains in two as-sprayed HVAF coatings (4L2 and 4L4 nozzle) were analyzed by XRD and compared to those in the gas-atomized powder, in a typical high-velocity oxy-fuel (HVOF) sprayed coating, in a typical high-velocity atmospheric plasma sprayed (HV-APS) coating and in a typical low-pressure plasma sprayed (LPPS) coating, manufactured according to standard procedures of the authors from the same powder as used in this work. In contrast to macrostrains (uniform) which are obtained by analysis of the peak positions, the microstrains (non-uniform) effect like local defects in the lattice. Figure 11(a) shows these microstrains which were obtained by peak broadening analysis of the x-ray diffractograms. In principle, residual stresses are a superposition of deposition stresses (due to the temperature difference between the impacting hotter particles and the colder substrate), thermal stresses (due to the thermal mismatch of coating and substrate materials) and peening stresses (due to the particle bombardment). The highest microstrains were found for the high-kinetic processes as here the particle velocities are the largest and the particle melting degrees are the lowest. The microstrains in the HVAF-sprayed samples are in between the HVOF and the HV-APS samples. On the other hand, complete melting of all the particles is obvious for the gas atomization process and for LPPS. This results in lower microstrains. Figure 11(b) shows that the largest amounts of β-phase were obtained for HV-APS and LPPS. It is assumed that the β-phase is forced to be dissolved to a large extent in the powder due to the high cooling velocity at gas atomizing and less precipitated in the colder high-
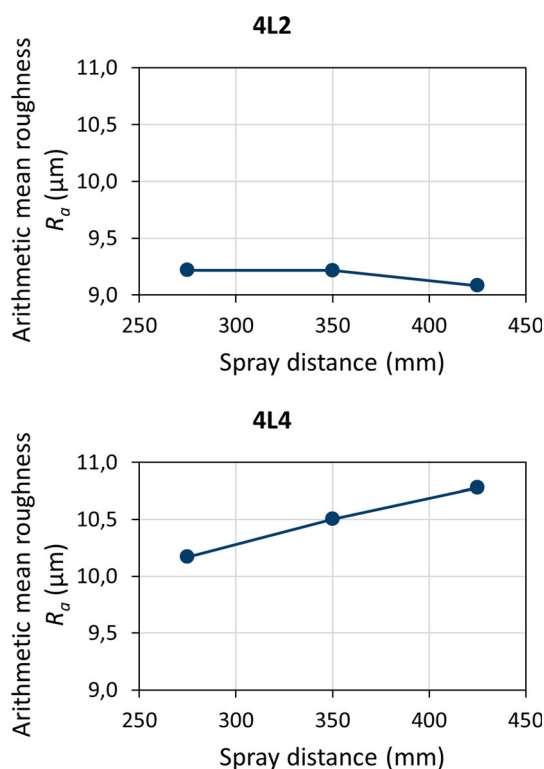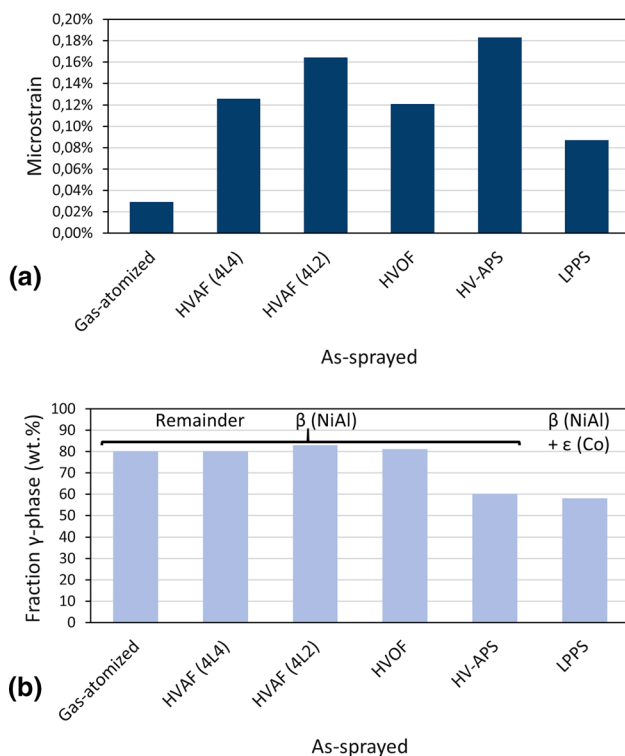
Fig. 11 Microstrains (a) and phase compositions (b) of two as-sprayed HVAF coatings (4L2 and 4L4 nozzle) in comparison with those in the gas-atomized powder, in a typical high-velocity oxy-fuel (HVOF) sprayed coating, in a typical high-velocity atmospheric plasma sprayed (HV-APS) sprayed coating and in a typical low-pressure plasma sprayed (LPPS) coating

kinetic processes HVAF and HVOF than in HV-APS and LPPS.

Conclusions

- The overall differences in the HVAF-sprayed microstructures obtained in this study with two different gun nozzles were small. The reason is that the gas velocities in the jet did not differ too much between both cases. The spray distance also did not have much influence, since the velocity variations in the jet were not large in the investigated range.
- Depending on their size, particles showed different melting grades and thus were either just thermally softened, partly (incongruently) molten or fully molten showing a viscous flow behavior. The characteristics of surface roughness and porosity basically depend on this.
- If the 4L2 nozzle was used, the particles were generally some faster than for the case of 4L4 nozzle. Obviously, the shock diamonds in the jet of the 4L2 nozzle did not affect the particle acceleration significantly.

- The maximum deposition efficiency slightly increased at higher particle velocities. The maximum particle velocity was found at 350-mm spray distance if the 4L4 nozzle was used, approx. 50 mm more downstream compared to the 4L2 nozzle (300 mm).
- The surface roughness was larger if the particle velocities were smaller. A leveling affect is assumed at higher particle impact velocities.
- The porosities showed the same trends like the surface roughness if the spray distance was varied. This suggests that similar mechanisms governed both properties.
- The oxygen content of the as-sprayed coatings was slightly higher in case of the 4L2 nozzle. Here, the gas density and thus the oxygen potential in the jet were larger compared to the 4L4 case. Oxygen was present in the jet with both nozzles due to the lean gas mixture.

As part of further research, TBC systems will be sprayed to investigate the durability of HVAF bondcoats with their specific microstructure, surface roughness and oxygen content as described in this work.

References

1. V. Champagne and D. Helfritch, The Unique Abilities of Cold Spray Deposition, *Int. Mater. Rev.*, 2016, **61**(7), p 437-455.
2. L.-M. Berger, Application of Hardmetals as Thermal Spray Coatings, *Int. J. Refract. Met. Hard Mater.*, 2015, **49**, p 350-364.

3. S. Yin, E.J. Ekoi, T.L. Lupton, D.P. Dowling and R. Lupoi, Cold Spraying of WC-Co-Ni Coatings Using Porous WC-17Co Powders: Formation Mechanism, Microstructure Characterization and Tribological Performance, *Mater. Des.*, 2017, **126**, p 305-313.

4. S. Kuroda, M. Watanabe, K. Kim and H. Katanoda, Current Status and Future Prospects of Warm Spray Technology, *J. Therm. Spray Technol.*, 2011, **20**(4), p 653-676.

5. P. Chivavibul, M. Watanabe, S. Kuroda, J. Kawakita, M. Komatsu, K. Sato and J. Kitamura, Effects of Particle Strength of Feedstock Powders on Properties of Warm-Sprayed WC-Co Coatings, *J. Therm. Spray Technol.*, 2011, **20**(5), p 1098-1109.

6. L.-M. Berger, R. Puschmann, J. Spatzier and S. Matthews, Potential of HVAF Spray Processes, *Therm. Spray Bull.*, 2013, **6**(1), p 16-20.

7. S. Joshi and P. Nylen, Advanced Coatings by Thermal Spray Processes, *Technologies*, 2019, **7**(4), p 79.

8. A. Verstak, V. Baranovski, AC-HVAF sprayed tungsten carbide: properties and applications, *Thermal Spray 2006: Building on 100 Years of Success*, B.R. Marple, M.M. Hyland, Y.-C. Lau, R.S. Lima, J. Voyer Eds., May 15-18, 2006 (Seattle, WA, USA), ASM International, pp 15-18

9. A.G. Fefekos, M. Gupta, S. Mahade, S. Björklund and S. Joshi, Effect of spray angle and substrate material on formation mechanisms and properties of HVAF sprayed coatings, *Surf. Coat. Technol.*, 2023, **452**, p 129115.

10. P. Khamsepour, C. Moreau and A. Dolatabadi, Effect of Particle and Substrate Pre-heating on the Oxide Layer and Material Jet Formation in Solid-State Spray Deposition: A Numerical Study, *J. Therm. Spray Technol.*, 2022 https://doi.org/10.1007/s11666-022-01509-7

11. R. Vaßen, Jülich Thermal Spray Center (JTSC)—a New Research and Innovation Infrastructure of Forschungszentrum Jülich, *CFI, Ceram. Forum Int.*, 2020, **97**(3-4), p E22-E25.

12. V.E. Belashchenko, V.E. Baranovski, Thermal spray systems, U.S. Patent No. 5,932,293, 1999

13. V. Baranovski, A. Verstak, High-velocity thermal spray apparatus and method of forming materials, U.S. Patent No. 6,245,390, 2001

14. V.E. Baranovski, A.V. Baranovski, Supersonic material flame spray method and apparatus, U.S. Patent Application No. 2011/0229649 A1, 2011

15. V. Matikainen, H. Koivuluoto, P. Vuoristo, J. Schubert and Š Houdková, Effect of Nozzle Geometry on the Microstructure and Properties of HVAF-Sprayed WC-10Co4Cr and Cr_3C_2-25NiCr Coatings, *J. Therm. Spray Technol.*, 2018, **27**(4), p 680-694.

16. J.G. Legoux, E. Irissou and C. Moreau, Effect of Substrate Temperature on the Formation Mechanism of Cold-Sprayed Aluminum, Zinc and Tin Coatings, *J. Therm. Spray Technol.*, 2007, **16**(5-6), p 619-626.

17. G. Mauer, R. Vaßen and D. Stöver, Comparison and Applications of DPV-2000 and Accuraspray-g3 Diagnostic Systems, *J. Therm. Spray Technol.*, 2007, **16**(3), p 414-424.

18. B. McKeon, G. Comte-Bellot, J. Foss, J. Westerweel, F. Scarano, C. Tropea, J. Meyers, J. Lee, A. Cavone, R. Schodl, M. Koochesfahani, Y. Andreopoulos, W. Dahm, J. Mullin, J. Wallace, P. Vukoslavčević, S. Morris, E. Pardyjak, A. Cuerva, Velocity, Vorticity, and Mach Number, *Springer Handbook of Experimental Fluid Mechanics*, C. Tropea, A.L. Yarin, J.F. Foss, Eds., Springer Berlin Heidelberg, 2007, p 215-471

19. S. Gordon, B.J. McBride, *Computer Program for Calculation of Complex Chemical Equilibrium Compositions and Applications - Analysis. NASA-Reference Publication, 1311 part 1*, NASA Lewis Research Center, 1994

20. S. Gordon, B.J. McBride, *Computer Program for Calculation of Complex Chemical Equilibrium Compositions and Applications - User's Manual and Program Description. NASA-Reference Publication 1311, part 2*, NASA Lewis Research Center, 1996

21. T. Varis, A. Mäkelä, T. Suhonen, J. Laurila and P. Vuoristo, Integrity of APS, HVOF and HVAF Sprayed NiCr and NiCrBSi Coatings Based on the Tensile Stress-Strain Response, *Surf. Coat. Technol.*, 2023, **452**, p 129068.

22. H.-B. Jung, J.-I. Park, S.-H. Park, H.-J. Kim, C.-H. Lee and J.-W. Han, Effect of the Expansion Ratio and Length Ratio on a Gas-Particle Flow in a Converging-Diverging Cold Spray Nozzle, *Met. Mater. Int.*, 2009, **15**(6), p 967-970.

23. N.-S. Cheng, Comparison of Formulas for Drag Coefficient and Settling Velocity of Spherical Particles, *Powder Technol.*, 2009, **189**(3), p 395-398.

24. H. Chen and T. Barman, Thermo-Calc and DICTRA Modelling of the β-Phase Depletion Behaviour in CoNiCrAlY Coating Alloys at Different Al Contents, *Comput. Mater. Sci.*, 2018, **147**, p 103-114.

25. H.-B. Xiong, L.-L. Zheng, L. Li and A. Vaidya, Melting and Oxidation Behavior of In-Flight Particles in Plasma Spray Process, *Int. J. Heat Mass Transfer*, 2005, **48**(25), p 5121-5133.

26. T. Mori, S. Kuroda, H. Murakami, H. Katanoda, Y. Sakamoto and S. Newman, Effects of Initial Oxidation on β Phase Depletion and oxidation of CoNiCrAlY bond coatings fabricated by warm spray and HVOF processes, *Surf. Coat. Technol.*, 2013, **221**, p 59-69.

27. G. Mauer, R. Vaßen and D. Stöver, Controlling the Oxygen Contents in Vacuum Plasma Sprayed Metal Alloy Coatings, *Surf. Coat. Technol.*, 2007, **201**(8), p 4796-4799.

28. G. Mauer, D. Sebold, R. Vaßen, E. Hejrani, D. Naumenko and W.J. Quadakkers, Impact of Processing Conditions and Feedstock Characteristics on Thermally Sprayed MCrAlY Bondcoat Properties, *Surf. Coat. Technol.*, 2017, **318**, p 114-121.

29. B. Rajasekaran, G. Mauer and R. Vaßen, Enhanced Characteristics of HVOF-Sprayed MCrAlY Bond Coats for TBC Applications, *J. Therm. Spray Technol.*, 2011, **20**(6), p 1209-1216.

30. V. Crespo, I.G. Cano, S. Dosta and J.M. Guilemany, The Influence of Feedstock Powders on the CGS Deposition Efficiency of Bond Coats for TBCs, *J. Alloys Compd.*, 2015, **622**, p 394-401.

31. G. Mauer and R. Vaßen, Plasma Spraying Porous Thermal Barrier Coatings with High Deposition Efficiency: A Solvable Dilemma?, *Surf. Coat. Technol.*, 2022, **451**, p 129070.

32. G. Mauer, Development of Plasma Parameters for the Manufacture of MCrAlY Bond Coats by Low-Pressure Plasma Spraying Using a Cascaded Torch, *Adv. Eng. Mater.*, 2022 https://doi.org/10.1002/adem.202200856